RESEARCH ARTICLE
SOLID EARTH: GEODESY AND GRAVITY

Earth and Planetary Physics
9: 1021–1036, 2025
doi: 10.26464/epp2025069

Physiography and basal melt rate of subglacial Lake 90°E

DanDan Li[1,2,3], Jun Liu[4], WeiFeng Hao[1,3], Sergey Popov[5], Lin Li[2], XiangBin Cui[2*], Fei Li[1,3,6*], ShiNan Lang[7], Bo Sun[2], and Martin Siegert[8]

[1]Chinese Antarctic Center of Surveying and Mapping, Wuhan University, Wuhan 430079, China;

[2]Polar Research Institute of China, Shanghai 200139, China;

[3]Key Laboratory of Polar Environment Monitoring and Public Governance, Wuhan University, Wuhan 430079, China;

[4]College of Urban Railway Transportation, Shanghai University of Engineering Science, Shanghai 201620, China;

[5]Polar Marine Geological Research Expedition (PMGRE), 24 Pobeda str., St. Petersburg, Lomonosov 198412, Russia;

[6]Department of Earth and Space Sciences, Southern University of Science and Technology, Shenzhen 518055, China;

[7]Faculty of Information Technology, Beijing University of Technology, Beijing 100124, China;

[8]Tremough House, University of Exeter, Penryn Campus, Penryn TR10 9FE, UK

Key Points:

- Lake 90°E, the second largest subglacial lake in Antarctica, has exhibited a stable ice surface elevation and boundaries over the past 20 years and has a maximum water depth of 320 m.
- Basal melt rates have remained low and stable over the last 400,000 years, ranging from 0.56 to 3.41 mm/yr, indicating thermodynamic equilibrium.
- The stability and unique conditions of the lake make it a prime candidate for future drilling, offering insights into lives in extreme subglacial environments.

Citation: Li, D. D., Liu, J., Hao, W. F., Popov, S., Li, L., Li, F., Cui, X. B., Lang, S. N., Sun, B., and Siegert, M. (2025). Physiography and basal melt rate of subglacial Lake 90°E. *Earth Planet. Phys.*, *9*(5), 1021–1036. http://doi.org/10.26464/epp2025069

Abstract: Lake 90°E in Antarctica encompasses an area of 2000 km^2, ranking it the second largest subglacial lake identified in the country by area, following Vostok Subglacial Lake. In this study, the overlying ice thickness and lake elevation of Lake 90°E were determined using airborne radio-echo sounding across two survey lines, conducted by the International Collaborative Exploration of the Cryosphere by Airborne Profiling in Princess Elizabeth Land (ICECAP/PEL) campaign during the 32nd Chinese National Antarctic Research Expedition (CHINARE 32, 2015–2016), and the depth of lake water was inversed by coupling with synchronous airborne gravity data. The analysis revealed a 15-m elevation increase in the ice sheet surface from the southeast to the northwest, correlating with a gradient in ice thickness that progresses from thin in the southeast to thick in the northwest. The maximum water depth of Lake 90°E is estimated as 320 m along the central line, bifurcated by a topographic ridge into two zones of varying depths, with exceptionally shallow water at its periphery. Thermodynamic modeling using data from two points along the survey lines indicated that melt rates at the ice–water interface have consistently been low over the last 400,000 years, varying between 0.56–0.95 mm/yr and 2.70–3.41 mm/yr, balanced by either basal freezing to the south or downstream water loss, thereby maintaining a thermodynamically stable state. Satellite imagery and altimetry data analyses identified no significant changes in the outline or elevation of the ice surface over the past 20 years. This study presents novel insights into the physiography and thermodynamic state of Lake 90°E, establishing a foundation for future drilling initiatives.

Keywords: airborne gravity; Antarctic subglacial lake; Lake 90°E; melt rate; radio-echo sounding

1. Introduction

Subglacial lakes, which require a thawed bed either at present or in the past (Hills et al., 2022), serve as vital windows into the historical dynamics of regional ice and climate. Sediments in these lakes also enhance our understanding of ice sheet evolution and paleoclimate variations (Siegert, 2000; Smith et al., 2018; Livingstone et al., 2022). The substantial water volumes discharged from subglacial lakes can act as a lubricant at the ice base, reducing basal shear stresses and promoting ice flow, which affects ice flow formation (Siegert and Ridley, 1998; Siegfried et al., 2016; Dow et al., 2018; Napoleoni et al., 2020; Maguire et al., 2021). Conversely, the erosional action of this water can alter basal topography, potentially inhibiting ice flow under certain conditions (Magnússon et al., 2007, 2010; Fricker et al., 2016). Research on

First author: D. D. Li, dandli@whu.edu.cn
Correspondence to: X. B. Cui, cuixiangbin@pric.org.cn
F. Li, fli@whu.edu.cn
Received 06 DEC 2024; Accepted 18 APR 2025.
First Published online 27 JUN 2025.

microorganisms detected in ice samples obtained through drilling operations supports the hypothesis that life could be sustained in such extreme environments (Karl et al., 1999; Bulat et al., 2004; Lavire et al., 2006). The melting of the ice ceiling and the water circulation within it could provide the mass and energy essential for sustaining life. Melting and freezing at the ice–water interface can be observed to some extent through changes in the surface elevation of the ice sheet above subglacial lakes (Wingham et al., 2006; Richter et al., 2008, 2022). Because circulation patterns are contingent on lake geometry (Studinger et al., 2004; Thoma et al., 2007; Couston and Siegert, 2021), investigating the physiography (the combination of glaciology, topography, and geology) and thermodynamic state of subglacial lakes is crucial in elucidating potential life forms, historical ice dynamics, and climatic conditions (Siegert, 2002).

Currently, the most common techniques used for the detection and characterization of subglacial lakes and their dynamics include satellite altimetry (Kapitsa et al., 1996; Howat et al., 2019), radio-echo sounding (RES; Kapitsa et al., 1996; Schroeder et al., 2013), gravity measurements (Studinger et al., 2004), and seismic surveys (Kapitsa et al., 1996). The discovery of the first subglacial lake in Antarctica occurred in 1967 via a RES profile close to Sovetskaya station (de Q. Robin et al., 1970). Moreover, a recent inventory identified 675 subglacial lakes on the continent (Livingstone et al., 2022). These lakes have been categorized into two groups, namely, stable and active. Stable lakes, which have predominantly been detected through RES, are typically found beneath thick ice in the interior of the ice sheet and within significant topographic troughs, such as the Vostok Subglacial Lake (VSL; Siegert et al., 2011). Active lakes are primarily identified through satellite altimetry and are often located near the ice margin (Livingstone et al., 2022).

Subglacial Lake 90°E (77.3789°S, 91.0805°E) ranks as the second largest lake in Antarctica by area (2000 km^2), following VSL (14,000 km^2). Despite its size, Lake 90°E is relatively underexplored and poorly understood. It is situated near the ice divide in the interior of East Antarctica and was first identified through an airborne survey conducted by the U.S. National Science Foundation between 2000 and 2001 (Studinger et al., 2003b; Siegert et al., 2005; Popov, 2022). At present, the sole study conducted on the physiography of Lake 90°E is the one by Bell et al. (2006), in contrast to the vast amount of research available on VSL. In Bell et al. (2006), Lake 90°E is characterized by a notably flat region in the ice, extending 123 km from north to south and reaching a maximum width of 20 km. The rectilinear morphology of Lake 90°E, coupled with its positioning along the western margin of the foreland basin—adjacent to the foothills of the Gamburtsev Subglacial Mountains—points to a tectonic origin for its encompassing trough (Bell et al., 2006). The presence of these deep, tectonically influenced subglacial lakes, which are likely to have remained stable across numerous glacial cycles because of the confining steep topography preventing water escape, suggests the potential for unique ecosystems to develop over prolonged periods (Bell et al., 2006). This characteristic makes Lake 90°E an exceptional natural laboratory for the study of life within subglacial lakes.

During the 32nd Chinese National Antarctic Research Expedition (CHINARE 32) in 2015–2016, the International Collaborative Exploration of the Cryosphere by Airborne Profiling in Princess Elizabeth Land (ICECAP/PEL) campaign was initiated to bridge the substantial data gap in Princess Elizabeth Land (PEL). This international airborne effort resulted in the collection of new RES and airborne gravity data over Lake 90°E. We have leveraged these newly acquired RES datasets to meticulously determine the thickness of the overlying ice sheet, the ice surface elevation, and the bedrock elevation of Lake 90°E along the survey lines. Given the inability of electromagnetic waves to penetrate water, water depths along the survey lines were deduced from synchronized airborne gravity data, using the RES-derived ice surface and bedrock elevations as constraints. In a novel approach to evaluating the stability of Lake 90°E, we analyzed two critical independent parameters for the first time: (1) the dynamics of the ice surface, as revealed through satellite imagery and altimetry data; and (2) the melt rate at the ice bottom, determined through thermodynamic modeling and RES-measured ice thickness. This study represents the first comprehensive analysis of Lake 90°E, Antarctica's second largest subglacial lake, and offers invaluable insights into its historical evolution. Furthermore, it enhances our understanding of the region's past ice dynamics and climatic conditions and lays the groundwork for subsequent subglacial lake drilling exploration endeavors.

2. Data and Methods

In 2015–2016, the ICECAP/PEL survey lines extended into the interior of the ice sheet, with two transects, denoted as R45a and R46a, strategically planned to traverse Lake 90°E in a southeast–northwest direction, covering both its central and marginal areas (Figure 1a). The profiles, labeled A–A′ along transect R46a and B–B′ along transect R45a (white lines in Figure 1a), spanning lengths of approximately 80 km and 45 km, respectively, were used in this analysis.

2.1 RES Data

The airborne RES utilizes a phase-coherent system operating at a central frequency of 60 MHz, with a bandwidth of 15 MHz and a peak power of 8 kW, enabling penetration through ice with a thickness greater than 4 km and achieving a vertical resolution of approximately 5.6 m (Cui XB et al., 2020). To enhance data quality, the raw RES data were processed using down-conversion, the removal of direct current offsets, pulse compression, and coherent and incoherent stacking. The processed data were then used to generate radargrams showing interfaces of the ice surface, internal layers, and bedrock. Each radar trace is precisely timestamped, allowing for correlation with global positioning system (GPS) times and positions with an accuracy exceeding 25 cm (Cui XB et al., 2018). We installed a Javad GPS receiver along with four antennas at key positions on the aircraft, including the center of gravity, tail, and both wings. The GPS data from the antenna located at the aircraft's center of gravity were utilized to interpret the RES data (Cui XB et al., 2018).

The delineation of the ice surface and ice–water or ice–bedrock interfaces was conducted along radargrams by using a semiauto-

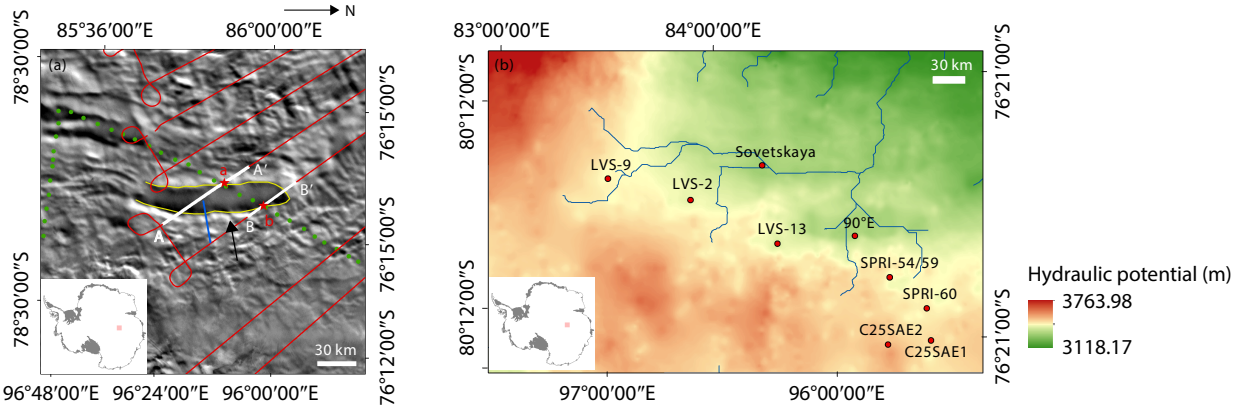

Figure 1. (a) Study area and ICECAP/PEL flight lines. The background is the Moderate Resolution Imaging Spectroradiometer (MODIS) mosaic. The airborne geophysical lines shown in red were surveyed in 2015–2016, and profiles A–A′ and B–B′ above Lake 90°E are depicted as white lines. The black arrow is the direction of the ice flow. The green points and blue line show free-air gravity measurements from the 1958 Soviet Antarctic Expedition and the extent of the RES transect in Bell et al. (2006), respectively. The yellow line shows the lake outline from Bell et al. (2006). (b) Hydraulic potential and simulated subglacial drainage pathways. The inset in each panel depicts the location of the study area.

matic method (Blankenship et al., 2011, 2012). The time difference between reflections from the ice surface and the ice–water or ice–bedrock interface was converted into ice thickness, utilizing a constant electromagnetic wave velocity of 1.68×10^8 m/s within the ice (Cui XB et al., 2020). Consistent with standardized glaciological protocols, firn corrections were intentionally omitted in this study. This methodological decision aligns with NASA IceBridge operational standards for Antarctic ice thickness retrievals (Blankenship et al., 2012). The ice surface elevation was determined by deducting the flight range from the flight altitude, which was measured using the airborne GPS data. The flight range itself was derived by multiplying the travel time of the reflection from the ice surface by the atmospheric electromagnetic wave velocity (3×10^8 m/s). The bedrock elevation was subsequently calculated by subtracting the ice thickness from the ice surface elevation.

2.2 Gravity Data

Gravity data were collected simultaneously with RES data along the transects R45a and R46a by using the GT-2A airborne gravimeter installed on the aircraft. The GT-2A is a three-axis stabilized scalar gravimeter designed to precisely measure accelerations attributable to the Earth's gravity and aircraft motion (Cui XB et al., 2018). The raw gravity measurements were corrected for aircraft motion acceleration and the Eötvös effect by using carrier-based differential GPS. In addition, free-air corrections were applied to derive the free-air gravity anomalies (Yang JJ et al., 2021). To minimize noise, a 150-s full-wavelength low-pass filter was implemented, resulting in an along-track resolution of 6.25 km and a data noise level of 1 mGal (Yang JJ et al., 2021).

Water depths along the A–A′ and B–B′ profiles of Lake 90°E were inversed using the Geosoft GMSys software package, which facilitates the simulation of geological formations and the calculation of model-generated gravity anomalies by utilizing a two-dimensional (2D) forward-modeling technique (Talwani et al., 1959). The algorithm numerically solves for the vertical (V) and horizontal (H) components of gravity anomalies by using the following analytical expressions:

$$\begin{aligned} V &= 2G\rho \sum_{i=1}^{n} a_i \sin\phi_i \cos\phi_i \\ &\left(\theta_i - \theta_{i+1} + \tan\phi_i \log_e \frac{\cos\theta_i(\tan\theta_i - \tan\phi_i)}{\cos\theta_{i+1}(\tan\theta_{i+1} - \tan\phi_i)}\right), \\ H &= 2G\rho \sum_{i=1}^{n} a_i \sin\phi_i \cos\phi_i \\ &\left(\tan\phi_i(\theta_{i+1} - \theta_i) + \log_e \frac{\cos\theta_i(\tan\theta_i - \tan\phi_i)}{\cos\theta_{i+1}(\tan\theta_{i+1} - \tan\phi_i)}\right), \end{aligned} \tag{1}$$

where G represents the gravitational constant, ρ denotes the density, a_i is the horizontal offset distance from the origin to the intersection point of the extrapolated polygon edge with the x-axis, ϕ is the angle between the extrapolated polygon edge and the x-axis, and θ is the angle between the line connecting the midpoint of the polygonal edge to the origin and the x-axis.

For this process, the surface and base of the ice sheet were maintained fixed at the ice surface and bedrock elevation observed by the RES. The water depths within the lake were determined based on the optimal match between the forward-modeled results and the recorded gravity data (Cochran et al., 2020). The following densities were assigned for the model: air at 0 g/cm^3; ice at 0.917 g/cm^3; water at 1 g/cm^3; and rock at 2.67 g/cm^3 (Schwabe et al., 2014; Millan et al., 2020).

2.3 Satellite Data

To analyze the activity of Lake 90°E over specified periods, we utilized data from the Ice, Cloud, and land Elevation Satellite (ICESat) missions (February 2003 to March 2009) and the subsequent Ice, Cloud, and land Elevation Satellite-2 (ICESat-2) missions (December 2019 to December 2023).

The repeat-track plane-fitting method was used to estimate elevation changes over the study area using ICESat data from 2003 to 2009. First, a grid is defined, and all the transit observation points within the grid are considered. Each point has associated elevation (H), longitude (E), latitude (N), and time (t) values. The differences

are calculated between the elevation, longitude, latitude, and time of each point and their respective mean values, denoted as dH, dE, dN, and dt. The relationships between these variables can be expressed in the form of a matrix equation:

$$\begin{bmatrix} \mathrm{d}H_1 \\ \vdots \\ \mathrm{d}H_n \end{bmatrix} = \begin{bmatrix} \mathrm{d}E_1 & \mathrm{d}N_1 & \mathrm{d}t_1 \\ \vdots & \vdots & \vdots \\ \mathrm{d}E_n & \mathrm{d}N_n & \mathrm{d}t_n \end{bmatrix} \cdot \begin{bmatrix} a_E \\ a_N \\ \mathrm{d}h/\mathrm{d}t \end{bmatrix} + \begin{bmatrix} r_1 \\ \vdots \\ r_n \end{bmatrix}, \tag{2}$$

where a_E represents the slope in the east–west direction, a_N represents the slope in the north–south direction, dh/dt is the elevation change rate (vertical movement velocity), and the residual r contains the remaining elevation change signals.

Let

$$\boldsymbol{y} = \begin{bmatrix} \mathrm{d}H_1 \\ \vdots \\ \mathrm{d}H_n \end{bmatrix}, \boldsymbol{B} = \begin{bmatrix} \mathrm{d}E_1 & \mathrm{d}N_1 & \mathrm{d}t_1 \\ \vdots & \vdots & \vdots \\ \mathrm{d}E_n & \mathrm{d}N_n & \mathrm{d}t_n \end{bmatrix}, \hat{\boldsymbol{X}} = \begin{bmatrix} a_E \\ a_N \\ \mathrm{d}h/\mathrm{d}t \end{bmatrix},$$

where $\boldsymbol{y}$ is the constant term column matrix of the error equation, $\boldsymbol{B}$ is the coefficient matrix of the error equation, and $\hat{\boldsymbol{X}}$ is the unknown column matrix.

On the basis of the above-mentioned equation, the error equation and least-squares estimation are as follows:

$$\boldsymbol{V} = \boldsymbol{B}\hat{\boldsymbol{X}} - \boldsymbol{y}, \tag{3}$$

$$\hat{\boldsymbol{X}} = (\boldsymbol{B}^{\mathrm{T}}\boldsymbol{P}\boldsymbol{B})^{-1}\boldsymbol{B}^{\mathrm{T}}\boldsymbol{P}\boldsymbol{y}, \tag{4}$$

where $\boldsymbol{V}$ is the column matrix of the corrections to the observed values and $\boldsymbol{P}$ is the weight matrix of the height differences. In this study, $\boldsymbol{P}$ is assumed to be 1.

After obtaining the parameter estimates, the precision of the parameters is calculated as follows:

$$\boldsymbol{Q}_{\hat{X}\hat{X}} = (\boldsymbol{B}^{\mathrm{T}}\boldsymbol{P}\boldsymbol{B})^{-1} = \begin{bmatrix} Q_{a_E}^2 & Q_{a_E a_N} & Q_{a_E,ht} \\ & Q_{a_N}^2 & Q_{a_N,ht} \\ \text{symmetric} & & Q_{ht}^2 \end{bmatrix}, \tag{5}$$

$$\sigma_0 = \sqrt{\frac{\boldsymbol{V}^{\mathrm{T}}\boldsymbol{P}\boldsymbol{V}}{n-t}}, \tag{6}$$

where $\boldsymbol{Q}_{\hat{X}\hat{X}}$ is the covariance matrix of the parameter estimates; Q_{a_E}, Q_{a_N}, and Q_{ht} are the auto-covariance matrices of, respectively, a_E, a_N, and dh/dt; σ_0 is the unit weight standard deviation; n is the number of observation points within the grid; and t is the number of parameters to be estimated (here, t = 3).

The error in the elevation change rate is given by

$$\sigma_{ht} = \sigma_0 Q_{ht}. \tag{7}$$

The elevation changes from 2019 to 2023 were analyzed using the ATL11 dataset from ICESat-2 Level 3B. This dataset is derived from repeated measurements, cross-track measurements, or both, enabling the detection of long-term elevation changes across various points on the ice sheet. Additionally, the data have undergone local topographic correction to enhance accuracy. Although the ATL11 dataset incorporates quality flags (e.g., "atl11_quality_summary") to exclude gross errors during its production, residual errors may still persist because of orbital perturbations and environmental disturbances. To ensure data reliability in this study, we applied a stringent quality control criterion by retaining only data points with a quality flag of 0 ("atl11_quality_summary = 0"). This approach minimizes the impact of potential errors and ensures the robustness of the elevation change analysis.

To mitigate the limitations of temporal coverage and the impacts of external environmental disturbances on Landsat imagery, we integrated data from Landsat 7 and 8 with the MEaSUREs (Making Earth System Data Records for Use in Research Environments) MODIS (Moderate Resolution Imaging Spectroradiometer) Mosaics of Antarctica (MOA) dataset. These datasets were used to manually digitize the surface outlines of Lake 90°E from 2001 to 2023, enabling consistent monitoring of its spatial dynamics.

The MODIS data utilized in this study comprise the MOA2004, MOA2009, and MOA2014 mosaics, which are composite datasets derived from image strips captured during the austral summer seasons of 2003–2004, 2008–2009, and 2013–2014, respectively. The specific acquisition periods for each mosaic are detailed in Table 1. These mosaics provide nearly cloud-free imagery at a spatial resolution of 125 m, with a base resolution ranging between 150 and 250 m (nominally 250 m at nadir). Their design prioritizes constrained solar illumination azimuth ranges, ensuring uniformity in lighting conditions critical for comparative analysis.

Table 1. Data sources used for the extraction of Lake 90°E surface outlines.

Data source	Time	Spatial resolution (m)
Landsat 7	2001.1	15
MOA2004 (Haran et al., 2021a)	2003.11–2004.2	125 × 125
MOA2009 (Haran et al., 2021b)	2008.11–2009.2	125 × 125
MOA2014 (Haran et al., 2018)	2013.11–2014.3	125 × 125
Landsat 8	2017.11	15
	2020.12	15
	2023.12	15

To align with the MODIS data characteristics, Landsat images were selectively acquired from corresponding austral summer periods, thereby maintaining temporal and illumination consistency. The data sources are detailed in Table 1. For each selected year, five independent digitizations of the lake outlines were conducted based on available imagery, and their averaged outline was used as the final representation of the lake extent for that year. This approach reduces the subjectivity of manual interpretation and enhances the robustness of temporal comparisons.

2.4 Ice Temperature Methods and Parameter Selection

To assess historical melt rate variations in Lake 90°E, we identified two points along the survey lines A–A′ and B–B′ with the maximum (a) and minimum (b) ice thicknesses to model the temperature distribution through the ice. The model uses a 1.5-dimensional advective–diffusive equation (Hills et al., 2022):

$$\frac{\partial T}{\partial t} = \frac{k}{\rho c}\frac{\partial^2 T}{\partial z^2} - w(z)\frac{\partial T}{\partial z} - u(z)\frac{\partial T}{\partial x} + \frac{Q}{\rho c}, \tag{8}$$

where T is the temperature, t is the time, and k is the thermal conductivity, which depends on the temperature and density. And c is the heat capacity, w is the vertical velocity, z is the height above bed, u is the longitudinal velocity, x is the longitudinal distance. For ice density,

$$k_i(T) = 9.828\,\mathrm{e}^{-5.7\times10^{-3}T}, \tag{9}$$

and for firn densities,

$$k = \frac{2k_i(T)\rho}{3\rho_i - \rho}, \tag{10}$$

where ρ_i is the density of ice;

$$c = 152.5 + 7.122T, \tag{11}$$

where c depends on temperature as well;

$$w = a\left(1 - \frac{p+2}{p+1}\zeta + \frac{1}{p+1}\zeta^{p+2}\right) + m, \tag{12}$$

and a is the accumulation rate (Bazin et al., 2013), p is the Lliboutry shape factor; m is the melt rate, and

$$m = \frac{1}{\Delta t}\frac{\rho c}{\rho_w L}\int_0^H (T - T_{\mathrm{pmp}})\mathrm{d}z, \tag{13}$$

$$T_{\mathrm{pmp}} = \gamma\rho g(H - z). \tag{14}$$

We assume a basal sliding case in our model, where the vertical velocity profile is linear ($p = 1000$). In addition, ζ is the normalized height above the bed, ρ_w is the density of water, L is the latent heat of fusion ($L = 3.33\times10^5$ J/kg), and H is the ice thickness. The ice thicknesses at points a and b, derived from RES data, were set as $H_a = 4127$ m and $H_b = 3762$ m, respectively. Temperature T_{pmp} is the temperature at the pressure melting point. The melting point depression constant γ is given as -7.42×10^8 K/Pa, and g is the gravitational constant ($g = 9.81$ m/s^2).

In addition to diffusion in the vertical dimension, this model adds an advection in the longitudinal direction, $u(z)\frac{\partial T}{\partial x}$, where $u(z)$ is the downstream velocity profile,

$$\frac{\partial T}{\partial x} \approx \frac{\mathrm{d}T_s}{\mathrm{d}x} + \frac{T - T_s}{2}\left(\frac{1}{H}\frac{\mathrm{d}H}{\mathrm{d}x} - \frac{1}{a}\frac{\mathrm{d}a}{\mathrm{d}x}\right), \tag{15}$$

and T_s is the temperature at the ice surface. The strain heat source is given by

$$Q = 2\tau_{xz}\varepsilon_{xz}, \tag{16}$$

where τ_{xz} is zero at the surface in the nonsliding case. In addition, the basal shear stress is equal to the driving stress,

$$\tau_b = \rho g H\frac{\mathrm{d}S}{\mathrm{d}x}, \tag{17}$$

where S is the ice surface elevation.

The strain rate profile, ε_{xz}, can be obtained by

$$\varepsilon_{xz} = A(T)\tau_{xz}^n, \tag{18}$$

where

$$A(T) = A^*\mathrm{e}^{\frac{-E}{R}\left(\frac{1}{T}-\frac{1}{T_r}\right)}, \tag{19}$$

where A^* is the rate factor constant ($A^* = 3.5\times10^{-25}$ /s·Pa^3), E is the activation energy ($E = 6\times10^4$ J/mol), R is the gas constant ($R = 8.3145$ J/mol·K), and T_r is the reference temperature ($T_r = 263$ K).

The surface boundary is fixed to the reconstructed paleo air temperature (Petit et al., 1999), and the bottom boundary is

$$\left[\frac{\partial T}{\partial z}\right]_0 = q_{\mathrm{geo}} + u_b\tau_b, \tag{20}$$

where u_b is the sliding velocity. Here, we approximate the sliding velocity by the surface velocity ($u_b = 1$ m/yr; Rignot et al., 2017) for the sliding case, and q_{geo} is the geothermal heat flux (GHF). Directly measuring the GHF beneath such extensive ice sheets proved to be a substantial challenge, rendering it poorly constrained. Consequently, in this study we approximated basal melt rates for Lake 90°E by using four distinct GHF datasets from published sources. Table 2 provides an overview of the sources of these datasets and the corresponding GHF values at points a and b.

Given the absence of ice core data specific to Lake 90°E and the similar climatic conditions between VSL and Lake 90°E, we referenced temperature and accumulation rate reconstructions from data on the Vostok Ice Core (Petit et al., 1999; Bazin et al., 2013). These ice core records, extending back 400 thousand years (kyr), facilitated the estimation of changes in the basal melt rate of Lake 90°E over the study period.

3. Lake Features and Geometry

3.1 Overlying Ice Thickness and Lake Surface Elevation

Strong, remarkably flat radio-wave reflections are hallmarks of RES records over subglacial water bodies deeper than 10 m (Gorman and Siegert, 1999). In contrast, weaker, undulating reflections are typically observed from the ice–bedrock interface at the base of the ice sheet (Siegert et al., 2005). At the central sections of the A–A′ and B–B′ profiles, RES captured reflections indicative of the ice–water interface, which is characteristic of subglacial lakes. In addition, the records revealed that both sides of the survey lines

Table 2. The GHF used to model the temperature distribution.

Dataset	Reference	Value (mW/m^2)	
		Point a	Point b
Satellite geomagnetic data	Purucker, 2013	45.21	45.45
Airborne magnetic observations	Martos et al., 2017	56.75	55.61
Seismic model	Shen WS et al., 2020	48.12	47.96
Airborne magnetic observations	Li L et al., 2021	68.33	71.7

displayed pronounced bed reflections, delineating the boundary of the lake and its adjacent topography (Figures 2a and 2d). The hydraulic potential was assessed using ice thickness and surface elevation data from MEaSUREs BedMachine Antarctica v3 (Morlighem et al., 2017). The analysis revealed a basin at the lake location featuring a flow outlet on the west side (Figure 1b), which underscores the significance of the lake as a water accumulation site.

The ice surface elevation at Lake 90°E exhibits an upward slope of 15 m from the southeast to the northwest on both the A–A′ and B–B′ profiles. The A–A′ profile clearly shows the transition from an ice–bedrock to an ice–water interface on the ice sheet surface elevation curve (represented by a blue line). Notably, a few kilometers southeast of the lake, a small trough approximately 11 m deep and 14 km long is observed on the ice sheet surface. Conversely, at the northwestern edge of the lake, a small peak, 8 m high and 5 km long, emerges. On the B–B′ profile, the transition from an ice–bedrock to an ice–water interface is apparent only on the northwest side, marked by a small peak. In the middle sections of the A–A′ and B–B′ profiles, the lake surface elevation is approximately –400 m and –150 m asl (above sea level), respectively, with minimal variation, in contrast with the complex and irregular subglacial topography surrounding the lake. The waterc surface or bedrock topography elevation curve (depicted by a red line) delineates the extent of Lake 90°E from (77.55°S, 91.10°E) to (77.24°S, 90.11°E) along profile A–A′, spanning 41.9 km, and from (76.97°S, 90.81°E) to (76.84°S, 90.39°E) along profile B–B′, covering 17.8 km. The ice sheet thickness overlying Lake 90°E exhibits thinning toward the southeast and thickening toward the northwest on both profiles. Specifically, the ice sheet thickness reaches 3950 m on the southeast and 4127 m on the northwest of the A–A′ profile. For the B–B′ profile, the ice thickness is 3762 m on the southeast and 3961 m on the northwest, indicating a lesser thickness compared with the A–A′ profile.

The crossover analyses of the 2015–2016 dataset used in this study revealed a root mean square error (RMSE) of approximately 24.2 m (Cui XB et al., 2018). The semiautomated techniques used to delineate the ice surface and the ice–water or ice–bedrock interface resulted in an extraction error equivalent to one pixel (approximately 5 m). Notably, the ice thickness estimates derived from RES in this study remained uncorrected for the firn layer. Quantification of firn corrections requires precise vertical density gradients, which demonstrate substantial regional variability across cryospheric provinces. Comparative analysis of three firn column structures reconstructed from ice core records indicated distinct correction magnitudes: +7 m for the Ross Ice Shelf, +10 m for the Central Greenland, and +15 m for the Vostok, central Antarctica (Dowdeswell and Evans, 2004). In this glaciological context, we implemented the Vostok-derived correction coefficient (+15 m) as the primary adjustment factor, which was justified by its glacio-stratigraphic similarity to the Lake 90°E subglacial environment.

3.2 Free-Air Gravity Anomaly and Water Depth

Along the A–A′ profile, a significant free-air gravity low was observed, with a magnitude approximately 70 mGal lower than the surrounding high values. The water depth on the A–A′ profile was determined using the topographical data acquired from the RES profile as a constraint for the gravity inversion (Figure 3b). The bathymetry estimated from the gravity inversion indicates that Lake 90°E, along profile A–A′, can be effectively segmented into two distinct regions by a topographical ridge. The southeastern section is substantially deeper, with a water depth of approximately 320 m, and covers a spatial area approximately 4 times larger than the relatively smaller northwestern section.

Along the B–B′ profile, the free-air gravity anomaly associated with Lake 90°E is approximately 50 mGal lower than the surrounding high values, which is marginally lower than the value recorded

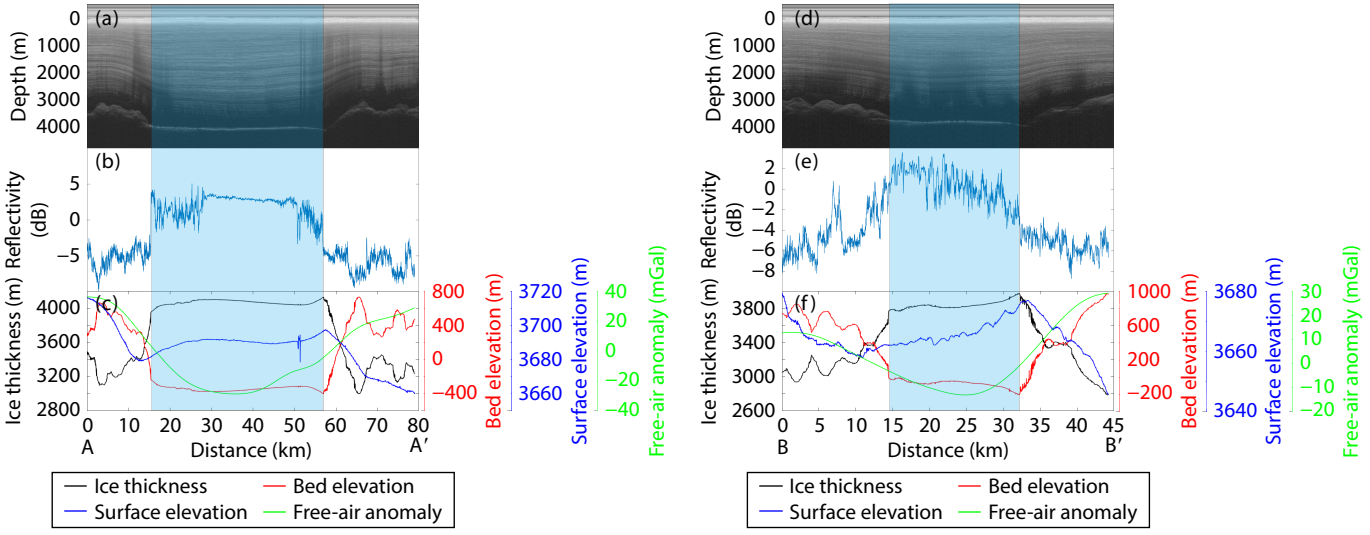

Figure 2. (a) 2D radio-echo sounding radargram, (b) reflectivity, and (c) ice thickness, bed elevation, surface elevation, and free-air anomaly curves along the profile A–A′ of Lake 90°E. (d) 2D radio-echo sounding radargram, (e) reflectivity, and (f) ice thickness, bed elevation, surface elevation, and free-air anomaly curves along the profile B–B′ of Lake 90°E. The vertical rectangles indicate the extent of the lake. See the location in Figure 1a.

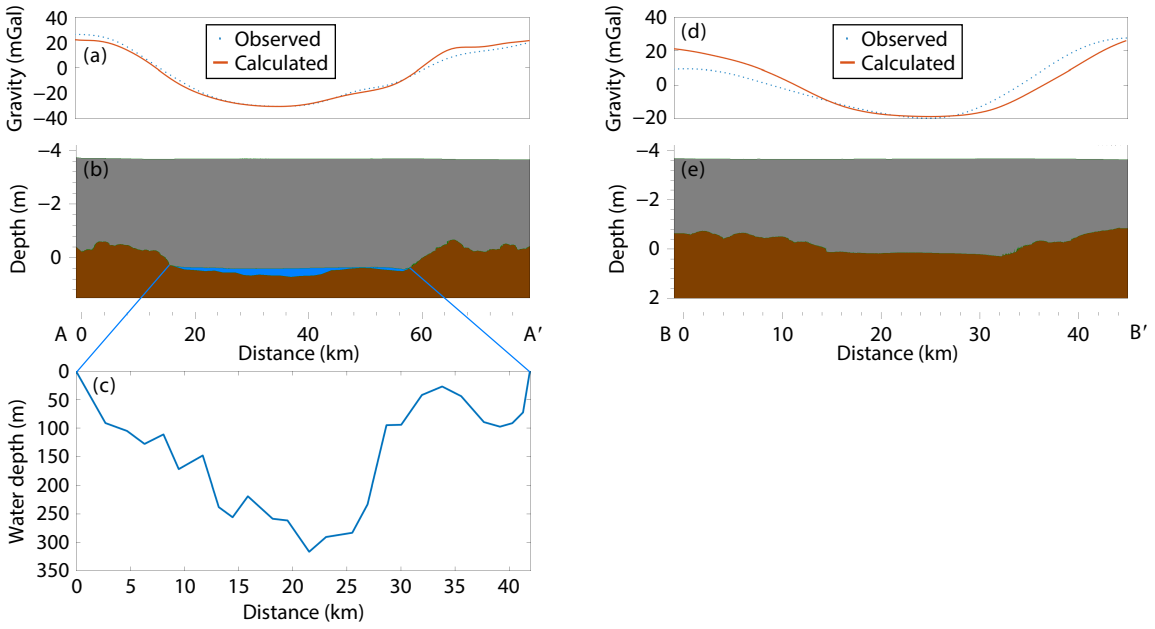

Figure 3. (a) Fitting of the observed gravity data to the forward-modeled data on profile A–A′. The blue points are the observed gravity data and the orange line is the gravity data obtained from forward modeling of the geological model. (b) The 2D gravity model along profile A–A′. The gray, blue, and brown blocks are ice, water, and bedrock, respectively. (c) Water depth distribution of Lake 90°E along profile A–A′. (d) Fitting of the observed gravity data to the forward-modeled data on profile B–B′. (e) The 2D gravity model along profile B–B′.

for the A–A′ profile (Figure 3d). When utilizing bedrock elevation data from RES as constraints for gravity inversion, the simulation failed to definitively determine the water depth of the lake.

Errors in gravity inversion primarily arise from instrumental and modeling inaccuracies. The airborne gravity data utilized in this study exhibited a noise level of 1 mGal. This 1 mGal uncertainty in the gravity data contributed to an approximate 20 m uncertainty in depth estimates based on the applied density contrast. The gravity model used a uniform bedrock density of 2.67 g/cm^3, disregarding the actual lateral variation in bedrock density. Consequently, water depth estimations fluctuated by 15–20 m for every 0.1 g/cm^3 deviation in bedrock density.

3.3 Ice Surface Dynamics

Elevation changes estimated using ICESat from October 2003 to March 2009 relative to November 2005 are depicted in Figure 4a. Detailed elevation changes along the tracks during this period are presented in Figure S1. Elevation changes recorded by ICESat from 2003 to 2009 varied from approximately −0.2 to 0.4 m. In addition, changes in the surface elevation of Lake 90°E in December 2023 relative to December 2019 estimated by ICESat-2 are illustrated in Figure 4c. The elevation changes every 3 months starting from December 2019 are depicted in Figure S2. Throughout the 4 years from 2019 to 2023, ICESat-2 documented elevation changes ranging from approximately −0.3 to 0.2 m.

The uncertainties associated with the elevation changes reported in this study primarily stem from instrument precision, errors in ground observations, inaccuracies in tidal adjustments, and discrepancies in model fitting. The distribution of these errors is elaborated in Figures 4b, 4d, and S3, revealing that the inaccuracies for ICESat do not exceed 0.14 m, whereas those for ICESat-2 remain below 0.06 m.

The outlines of Lake 90°E depicted in Figure 4e indicate that the outlines of Lake 90°E exhibited relative stability, with no evident trend of expansion or contraction from 2001 to 2023. To assess uncertainty introduced by manual digitization, we quantified digitization consistency by using the mean of the shortest distances between repeatedly extracted lake outlines. The results revealed an average deviation range of approximately 438 to 735 m across all years. Notably, MODIS-based digitizations demonstrated the lowest deviations (~438–533 m), followed by Landsat 8 (~548–650 m), with Landsat 7 exhibiting the largest uncertainty (~735 m). The MOA products are mosaics of the Antarctic ice sheet, designed to provide nearly cloud-free views of the ice sheet, ice shelves, and outcrop surfaces for land areas north of 60°S, which likely contributes to the superior clarity and lower uncertainty observed in MODIS-based digitizations. Nevertheless, the results collectively indicated that the digitization methodology maintained acceptable consistency across both sensors and temporal scales.

4. Basal Melt Rate

Figures 5c and 5d illustrate the spatiotemporal characteristics of basal melt rates at points a and b, calculated using four distinct GHF datasets. Notably, except for the dataset from Li L et al. (2021), which yielded higher melt rates at point b (2.70–3.41 mm/yr), the remaining three datasets consistently showed higher average melt rates at point a (mean difference ≈ 0.33 mm/yr). Among these, the GHF data from Li L et al. (2021), derived from airborne magnetic anomaly inversions (68.33–71.70 mW/m^2), produced the maximum melt rates (a: 2.59–3.25 mm/yr; b: 2.70–3.41 mm/yr). In contrast, the satellite magnetic dataset from Purucker (2013; 44.87–45.45 mW/m^2)

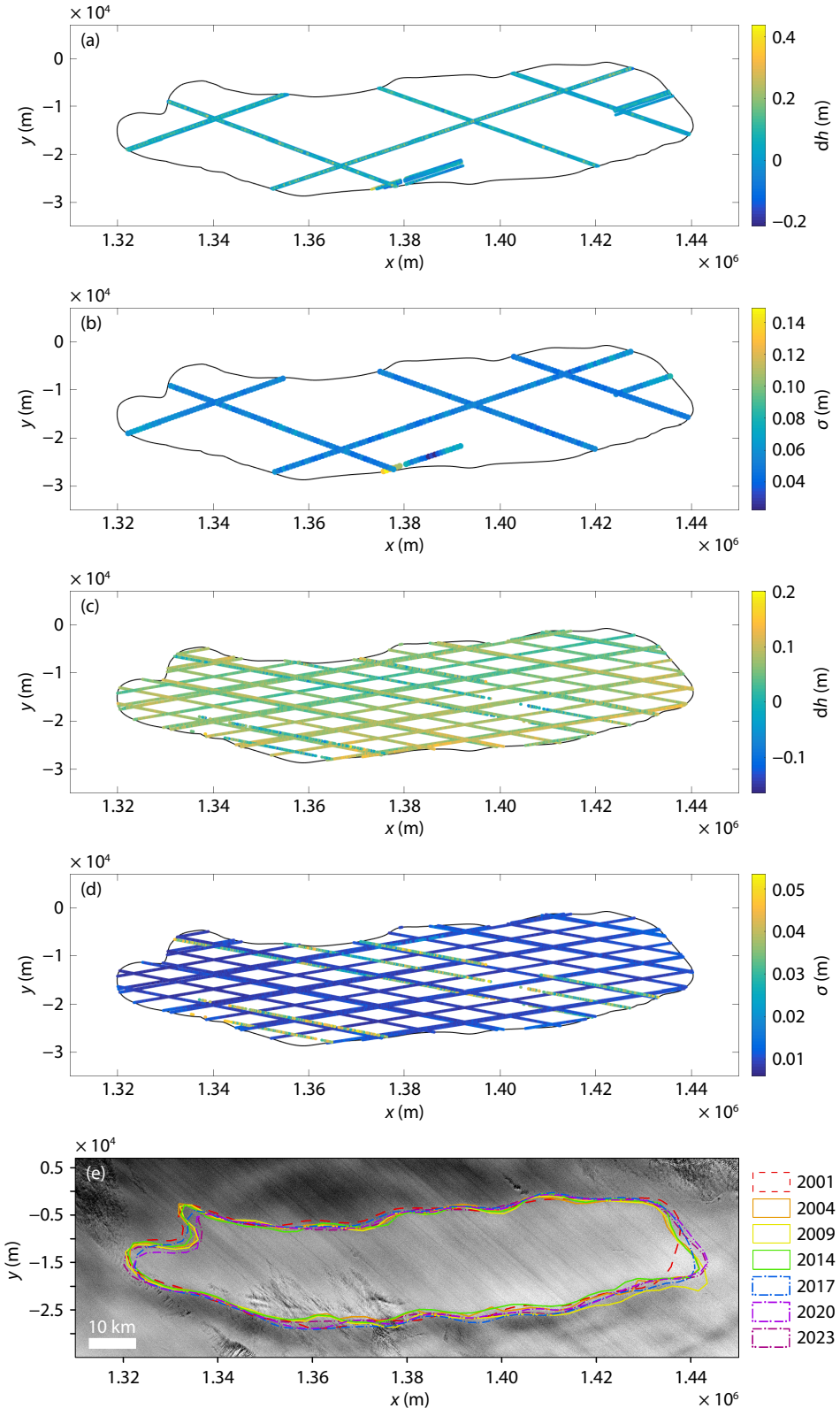

Figure 4. (a) Changes in ice surface elevation and (b) their uncertainties from October 2003 to March 2009 relative to November 2005 based on ICESat. (c) Ice surface elevation changes and (d) their uncertainties in December 2023 relative to December 2019 based on ICESat-2. The black line is the location of Lake 90°E. (e) Outlines of Lake 90°E from 2001 to 2023. The background is from Landsat 8 in 2023.

yielded the lowest values (a: 0.80–1.17 mm/yr; b: 0.56–0.95 mm/yr). Across the span of the reconstructed paleoclimate history, the basal melt rates at points a and b, inferred from varying GHF data, demonstrate a positive and upward trend. Notably, there were transient reductions in melt rates during interglacial periods, specifically before 130, 220, and 320 kyr ago.

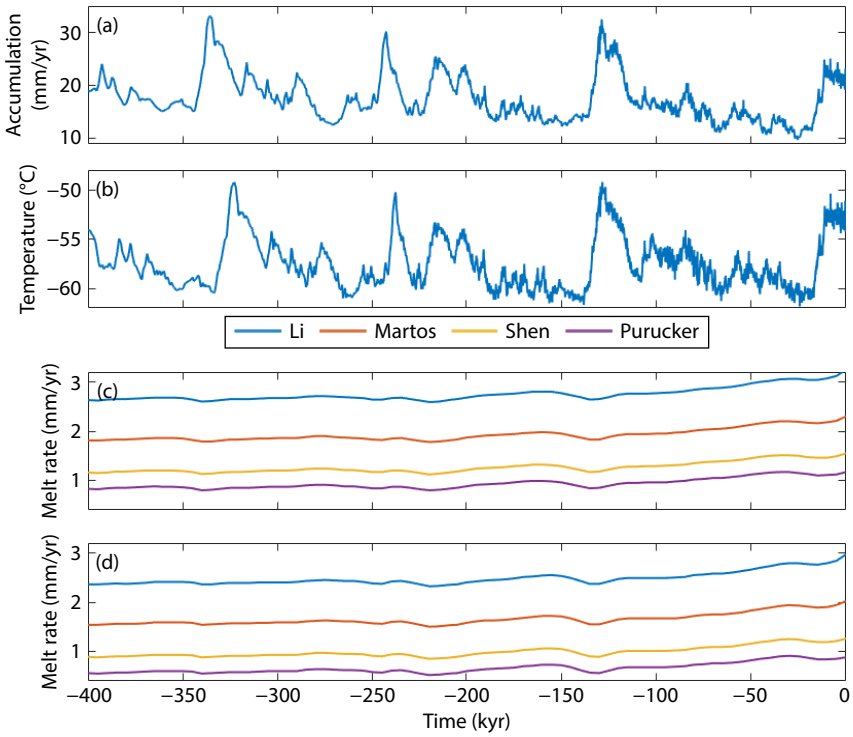

Figure 5. Accumulation rate (a) and temperature (b) from the Vostok Ice Core (Petit et al., 1999; Bazin et al., 2013). (c) Modeled melt rates of point a based on different GHF datasets. (d) Modeled melt rates of point b based on different GHF datasets.

The errors in estimating basal melt rates are a result of the poorly constrained GHF and the ice sheet thickness value obtained from the RES. In the case of point a, for example, the omission of firn correction in calculating ice sheet thickness contributed to a decrease in melt rates by approximately 0.01 mm/yr when using the dataset from Martos et al. (2017). In addition, using the most recent reconstructed Vostok Ice Core data for temperature and accumulation rates introduced further uncertainties to the melt rate calculations. In this context, we analyzed the historical climatic conditions at points a and b against the Vostok Ice Core data for the recent decades (1980–2022). We determined similar temperatures at points a and b. The RMSE for the temperature discrepancy with the Vostok Ice Core was approximately 2.8 °C for point a and 2.9 °C for point b. At location a within the thickest sector of the ice sheet, a temperature perturbation of 2.8 °C induced a proportional change in the basal melt rate of ±0.16 mm/yr (Figure 6a). This sensitivity demonstrates a magnitude comparable to that observed at point b, where a 2.9 °C temperature variation corresponds to a ±0.17 mm/yr melt rate modification (Figure 6b). Notably, both locations exhibited symmetrical thermal responses despite their spatial separation. Accumulation revealed distinct characteristics between the sites. Relative to the Vostok Ice Core, the RMSE of accumulation rate discrepancies measured 10.5 mm/yr at point a versus 9.05 mm/yr at point b. These accumulation variations demonstrate nonlinear coupling with basal processes. Specifically, a +10.5 mm/yr accumulation anomaly at point a produced a −0.36 mm/yr melt rate reduction, whereas equivalent negative forcing (−10.5 mm/yr) generated a +0.46 mm/yr melt acceleration (Figure 6a). This response asymmetry persisted at point b, where ±9.05 mm/yr accumulation changes yielded −0.32/+0.39 mm/yr melt rate modifications, respectively (Figure 6b). The comparative analysis revealed two critical patterns. First, temperature forcing generated symmetrical basal responses (±0.16–0.17 mm/yr), in contrast with the asymmetrical accumulation impacts. Second, accumulation rate perturbations exerted a disproportionately greater influence on basal melt dynamics than did temperature changes.

5. Discussion

5.1 Geometry of Lake 90°E

The RES data utilized by Bell et al. (2006) covers only the eastern side of Lake 90°E and consequently does not provide a comprehensive view of the ice thickness (Figure 1a). This study updates and augments the information on ice surface elevation, ice thickness, and bedrock elevation for the central and northern sides of Lake 90°E, using the most recent RES data. The presence of troughs and peaks on the ice surface in Lake 90°E underscores the substantial impact of large subglacial lakes on the surface topography of the ice sheet (Kapitsa et al., 1996). This effect arises from variations in ice dynamics, transitioning from grounded to floating and then to regrounded states (Mayer and Siegert, 2000; Kotlyakov et al., 2011; Fricker et al., 2016). The ice thickness at the southeastern end of the A–A′ profile is 3950 m, closely matching the eastern thickness of 3980 m reported by Bell et al. (2006). Conversely, this study calculated the ice thickness at the northwest end of the A–A′ profile as 4127 m, exceeding the western thickness of 4032 m projected by Bell et al. (2006) and aligning with measurements on the north side of the VSL (Studinger et al., 2003a). The discrepancy between the findings of this study and previously published results for the west side of Lake 90°E can be attributed to variations in the RES survey line locations and the

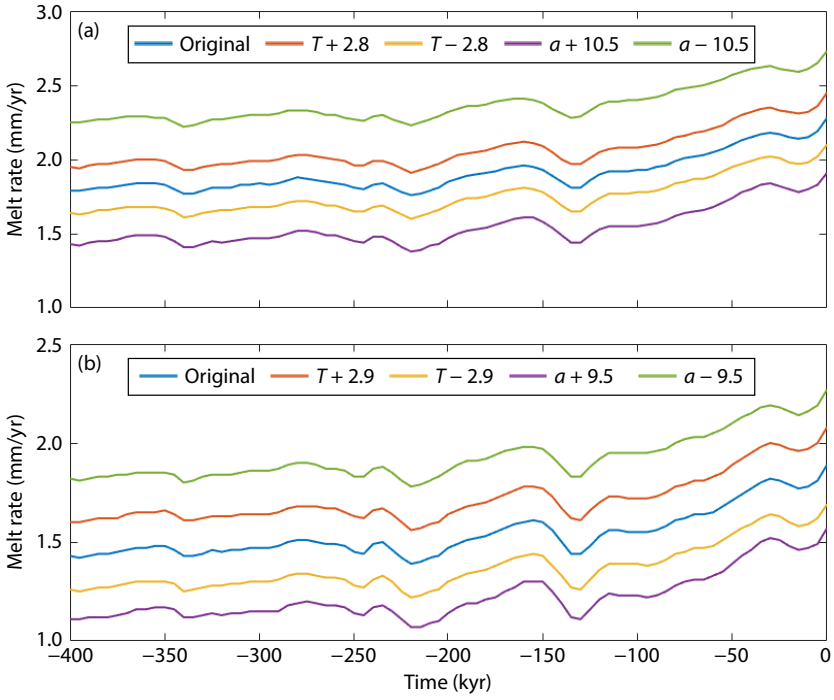

Figure 6. Variations in melt rates at point a (a) and point b (b) under different temperatures (*T*) and accumulations (*a*).

methodologies used for estimating ice thickness in Bell et al. (2006), which inferred the ice thickness on the 90°E west side from available RES data.

The water depth estimated in this work was 320 m, which shows a remarkable disparity compared with the 900 m water depth reported by Bell et al. (2006). The free-air gravity anomaly observed on the A–A′ profile in this study exhibited a slightly lower magnitude by approximately 10 mGal compared with the 80 mGal gravity anomaly low reported by Bell et al. (2006). According to our previous calculations, in our gravity model, an error of 1 mGal will bring about an uncertainty of ~20 m in the depth estimate. Another potential source of this variation is the lack of synchronization between the gravity and RES data in Bell et al. (2006), potentially resulting in inaccuracies in the water depth estimations. In this study, we performed an analysis by constraining the gravity inversion process along the A–A′ profile with the radar-derived bedrock interface from the B–B′ profile. This methodological experiment yielded a maximum water depth estimate of 675 m, representing a 355 m increase compared with the synchronized data-constrained result of 320 m presented in our primary analysis. This substantial discrepancy highlights the critical sensitivity of subglacial bathymetry inversions to spatiotemporal data consistency, particularly regarding the temporal alignment between radar bedrock mapping and airborne gravity surveys.

On the northern side of Lake 90°E, features characteristic of subglacial lakes are identifiable on the B–B′ profile, yet the presence of a water layer, as might be expected, was not confirmed through gravity inversion. This discrepancy arose because RES is capable of detecting water layers exceeding 10 m in thickness, whereas the noise associated with gravity data in this study introduced an uncertainty of approximately 20 m in depth estimations. Consequently, any water layer present on the B–B′ profile may be too thin to fall within the detection capabilities of gravity measurements. Additionally, the gravity inversion process was based on simplified assumptions, such as a uniform bedrock density of 2.67 g/cm^3, which deviates from the actual geological situation. And a deviation of 0.1 g/cm^3 in bedrock density can change the water depth estimation by 15–20 m. However, data are currently lacking in this study area to effectively constrain the distribution of bedrock density, increasing the difficulty of accurately determining the water layer. Therefore, both data noise and the deviation of bedrock density in the model assumptions have influenced the judgment of the water layer. Furthermore, the reflectivity observed on the B–B′ profile is lower than that on the A–A′ profile, suggesting that the water layer on the former is thinner than that on the latter (Carter et al., 2009; Young et al., 2016). On the other hand, Lake 90°E, a tectonically formed subglacial lake, occupies a structural trough shaped by regional crustal deformation. The uniform basal topography across its A–A′ and B–B′ profiles (Figure 2) reflects consistent tectonic controls on basin evolution. Although this geomorphic symmetry does not confirm subglacial water beneath B–B′, it supports hydrogeologic inference: the confirmed presence of water under A–A′, coupled with the shared tectonic architecture, suggests analogous lithospheric conditions for water storage at B–B′. This morphotectonic consistency enhances the probability of subglacial aqueous phases in spatially linked basins under similar stress regimes. An alternative hypothesis suggests that there may be no water beneath the B–B′ profile, raising concerns about the accuracy of deducing the extent of subglacial lakes from ice sheet surface observations. For example, satellite imagery initially indicated that Lake Snow Eagle covered an area of 1250 km^2 (Jamieson et al., 2016), whereas subsequent airborne RES measurements disclosed its true extent to be only 370 km^2 (Yan S et al., 2022). Reflectivity is also likely to be overestimated, which could result in the misclassification of subglacial lakes (Killingbeck et al., 2024).

To enhance the accuracy of detecting a thin water layer, future studies should consider utilizing higher precision gravity measurement instruments. Such advances would effectively reduce data noise, improve measurement accuracy, and minimize depth-estimation uncertainties caused by measurement errors. Consequently, this would increase the likelihood of identifying a thin water layer with greater confidence. Additionally, integrating multiple geophysical exploration methods is essential for a more comprehensive analysis. In particular, seismic exploration plays a crucial role in this context. Given that seismic waves exhibit distinct propagation characteristics in different media, seismic surveys can provide more detailed insights into subsurface structures. Seismic exploration can verify the existence of a thin water layer from different angles, offering stronger evidence for judging the presence of a thin water layer.

5.2 Stability Analysis of Lake 90°E

This study utilized the most recent satellite data and thermodynamic modeling to present an inaugural analysis of the stability of Lake 90°E. Observations from ICESat and ICESat-2 indicate that elevation changes within Lake 90°E are less than 0.4 m. This magnitude of change is smaller than the elevation fluctuations observed in stable Lake CECs (Centro de Estudios Científicos), which serves as a significant marker of stability (Rivera et al., 2015).

The ice core data (Figures 5a and 5b) exhibit parallel patterns of change in the accumulation rate and temperature, yet they diverge in their effects on the basal melt rate. In particular, an increase in the accumulation rate reduces the basal melt rate, whereas a temperature rise enhances it. In the applied model, changes in the accumulation rate exert a more pronounced impact on the melt rate, resulting in a melt rate trend that is essentially inverse to the accumulation rate. Figures 5c and 5d demonstrate that the basal melt rates have consistently been positive and have gradually been rising over the past 400 kyr, suggesting ongoing melting of the Lake 90°E bed, with an intensifying degree of melts from the past to the present. Nonetheless, this melting process is balanced by snow accumulation (Duxbury et al., 2001). Positioned within a subglacial "lake district," the meltwater of Lake 90°E could slowly disperse into adjacent lakes with lower hydraulic potential, such as Lake Sovetskaya to the west, via subglacial channels (Figure 1b). Evidence also suggests potential connectivity between Lake 90°E and VSL through these channels (Klokočník et al., 2018). Moreover, Lake 90°E has seen temporary reductions in melt during several interglacial periods, characterized by high accumulation rates. Increased accumulation rates contribute to ice sheet thickening and enhanced melting, resulting in brief periods of reduced melting swiftly followed by a resurgence to higher melting phases.

6. Conclusions

During the ICECAP/PEL campaign in 2015–2016, an airborne geophysical survey was conducted over PEL. This study leverages the most recent geophysical data to present novel findings for Lake 90°E by encompassing measurements of the overlying ice thickness, lake surface elevation, shoreline delineation, water depth, and bedrock elevation along the A–A′ and B–B′ profiles. Furthermore, this study introduces an inaugural analysis of the ice surface dynamics and basal melt rates by integrating these findings with satellite remote sensing data to gain a comprehensive understanding of the lake.

The ice surface above Lake 90°E along the A–A′ and B–B′ profiles exhibits an upward slope of 15 m from the southeast to the northwest, with a trough and a peak identified on the surface. Notably, the ice thickness in the central area of the lake (3950–4127 m) is greater than that at the lake's periphery (3762–3961 m). In addition, the overlying ice sheet thickness decreases in the southeast and increases in the northwest along both profiles. These observations suggest that the overlying ice sheet forms an inclined cover over Lake 90°E, and this inclination likely facilitates water circulation within the lake.

Gravity inversion analysis revealed that the central portion of Lake 90°E has a water depth of approximately 320 m and is bifurcated by a ridge into two distinct segments. The southeastern segment is 4 times longer than its northwestern counterpart along the A–A′ profile, a configuration that mirrors the structure of VSL. This spatial arrangement significantly influences water circulation within Lake 90°E, potentially leading to varied patterns of melting and freezing. At the northern edge of the lake, the water depth is notably shallow, estimated to be only 10–20 m.

The change in ice surface height over Lake 90°E from 2003 to 2009 and 2019 to 2023 indicates a minimal elevation variation of less than 0.4 m. Satellite imagery analysis over the period from 2001 to 2023 demonstrates that the ice outlines of the lake have remained relatively unchanged throughout this time frame. It can be inferred based on these observations that Lake 90°E has not undergone substantial infilling or water discharge within this period, suggesting a state of stability.

Thermodynamic modeling indicates that the basal melt rate of Lake 90°E has been positive and on an upward trend over the past 400 kyr, suggesting that the East Antarctic ice sheet may have undergone increasing melting and ice loss during this timeframe. Notably, the basal melt rate exhibited temporary decreases during several interglacial periods, particularly before 130, 220, and 320 kyr. Depending on the GHF datasets and ice thickness utilized, the melt rate across 400 kyr ranged from 2.70 to 3.41 mm/yr for the highest estimates and 0.56 to 0.95 mm/yr for the lowest. The thermodynamically stable conditions of Lake 90°E, combined with its tectonic origins, indicate its capacity to support the development of unique ecosystems, making it a prime candidate for future exploratory drilling. Therefore, the basal melt rate calculations for Lake 90°E can serve as a critical factor in selecting sites for future subglacial lake drilling endeavors.

Acknowledgments

We are grateful for support from the National Natural Science Foundation of China under Grants 42376253, 42201489, and 42474056 and Shanghai Science and Technology Development Funds under Grant 21ZR1469700. We thank the Snow Eagle 601 crew from Kenn Borek Air (KBA) and ICECAP/PEL members for supporting the field data acquisition.

Disclosure Statement

The authors declare no conflict of interest.

Supplementary Materials

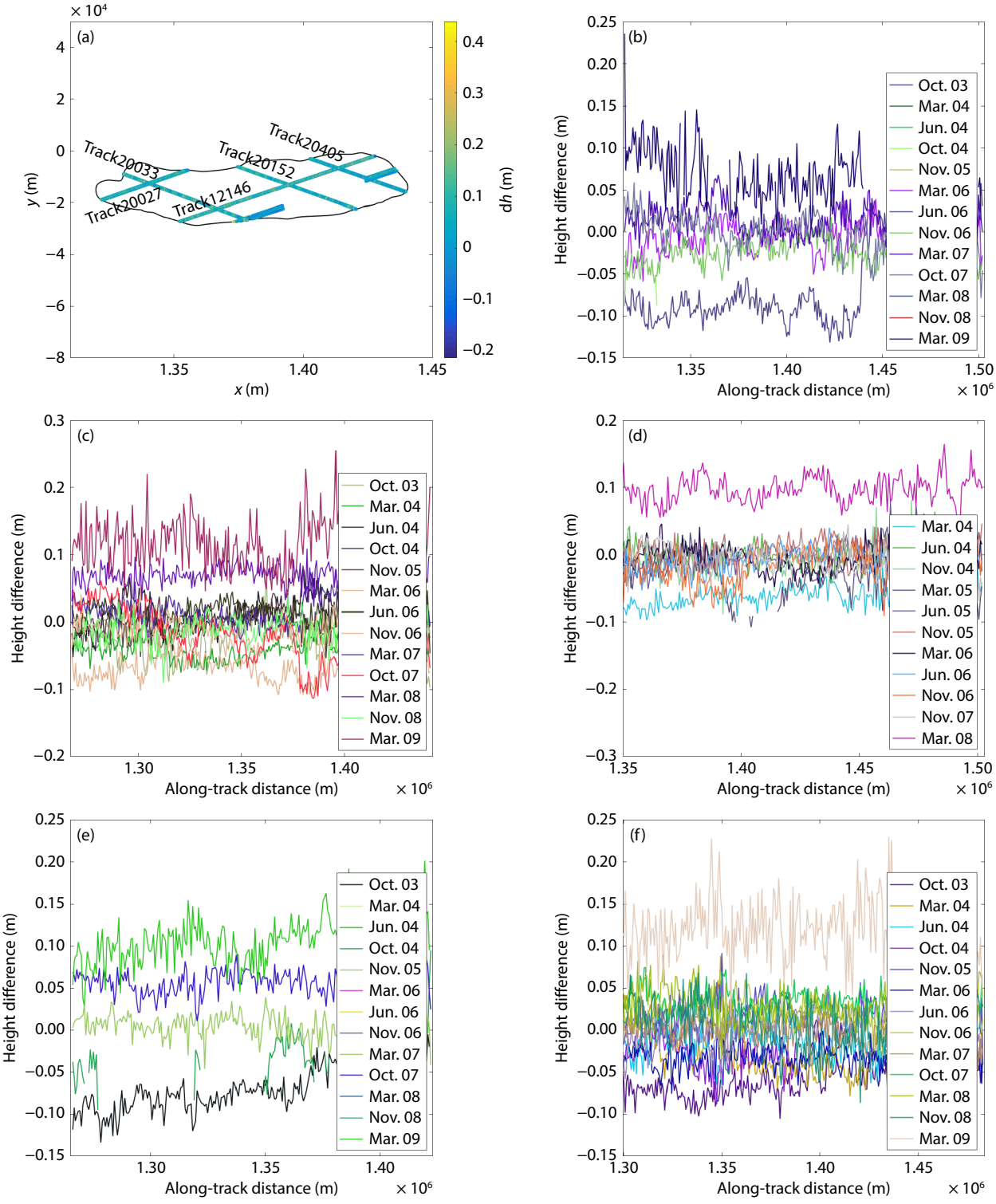

Figure S1. (a) Changes in ice surface elevation between October 2003 and March 2009 compared with the baseline of November 2005 analyzed using ICESat data. The black line is the outline of Lake 90°E. (b–f) The height difference profile of the tracks from October 2003 to March 2009 in comparison with the baseline of November 2005 derived from ICESat data. (b) Track20033, (c) Track20152, (d) Track20405, (e) Track20027, (f) Track12146.

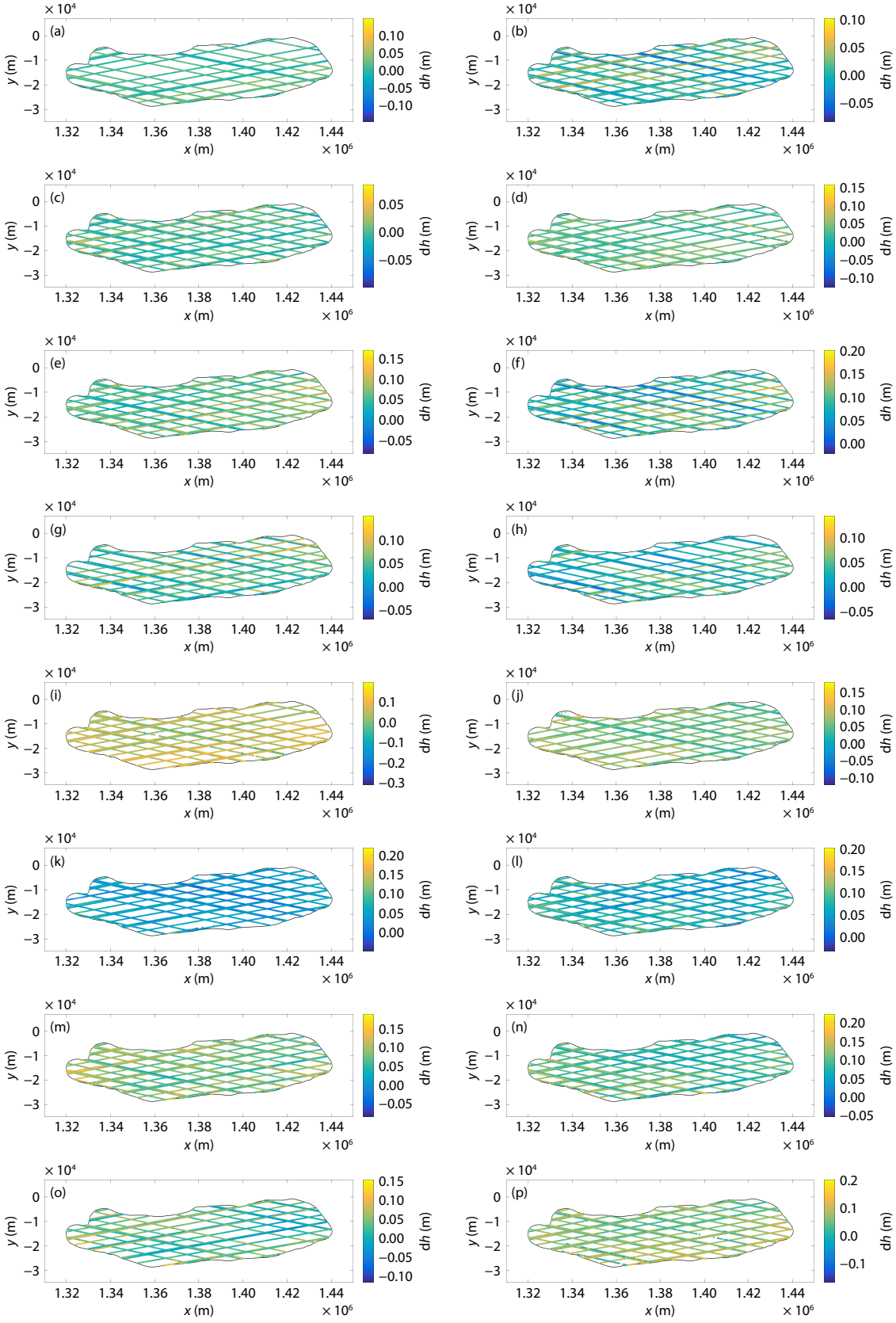

Figure S2. Ice surface elevation changes during (a) March 2020, (b) June 2020, (c) September 2020, (d) December 2020, (e) March 2021, (f) June 2021, (g) September 2021, (h) December 2021, (i) March 2022 (j) June 2022, (k) September 2022, (l) December 2022, (m) March 2023, (n) June 2023, (o) September 2023, and (p) December 2023, with December 2019 serving as the reference point. These changes were quantified using data derived from ICESat-2.

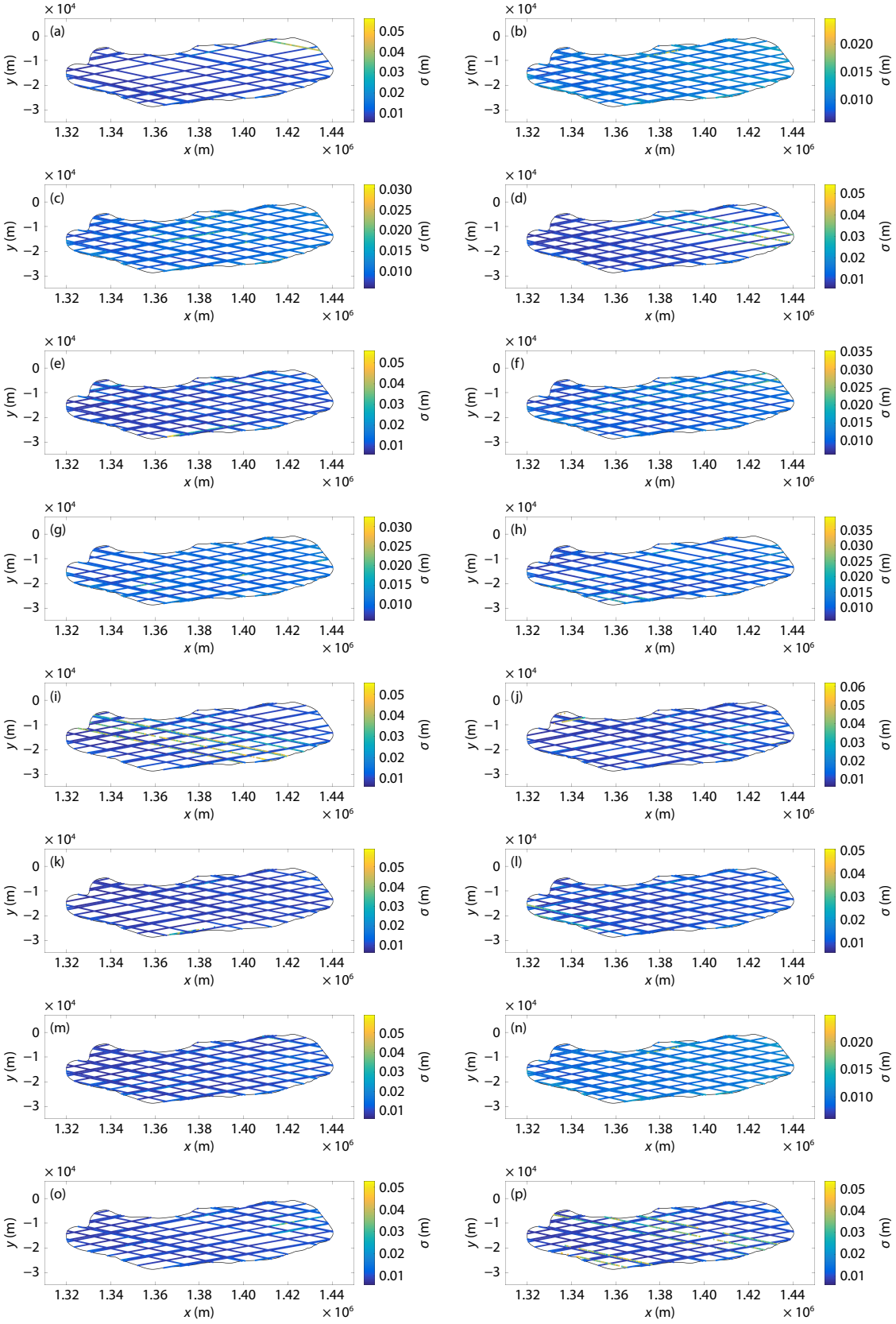

Figure S3. Uncertainty associated with changes in ice surface elevation during (a) March 2020, (b) June 2020, (c) September 2020, (d) December 2020, (e) March 2021, (f) June 2021, (g) September 2021, (h) December 2021, (i) March 2022 (j) June 2022, (k) September 2022, (l) December 2022, (m) March 2023, (n) June 2023, (o) September 2023, and (p) December 2023, using December 2019 as the reference point. These uncertainties were assessed using data from ICESat-2.

References

Bazin, L., Landais, A., Lemieux-Dudon, B., Mahamadou Kele, H. T., Veres, D., Parrenin, F., Martinerie, P., Ritz, C., Capron, E., … Wolff, E. (2013). An optimized multi-proxy, multi-site Antarctic ice and gas orbital chronology (AICC2012): 120–800 ka. *Climate Past*, *9*(4), 1715–1731. https://doi.org/10.5194/cp-9-1715-2013

Bell, R. E., Studinger, M., Fahnestock, M. A., and Shuman, C. A. (2006). Tectonically controlled subglacial lakes on the flanks of the Gamburtsev Subglacial Mountains, East Antarctica. *Geophys. Res. Lett.*, *33*(2), L02504. https://doi.org/10.1029/2005gl025207

Blankenship, D. D., Kempf, S. D., Young, D. A., Richter, T. G., Schroeder, D. M., Greenbaum, J. S., Holt, J. W., van Ommen, T., Warner, R. C., … Siegert, M. J. (2011). IceBridge HiCARS 1 L2 Geolocated Ice Thickness. (IR1HI2, Version 1). [Data Set]. Boulder, Colorado, USA: NASA National Snow and Ice Data Center Distributed Active Archive Center. https://doi.org/10.5067/F5FGUT9F5089

Blankenship, D. D., Kempf, S. D., Young, D. A., Richter, T. G., Schroeder, D. M., Ng, G., Greenbaum, J. S., van Ommen, T., Warner, R. C., … Siegert, M. J. (2012). IceBridge HiCARS 2 L2 Geolocated Ice Thickness. (IR2HI2, Version 1). [Data Set]. Boulder, Colorado, USA: NASA National Snow and Ice Data Center Distributed Active Archive Center. https://doi.org/10.5067/9EBR2T0VXUDG

Bulat, S. A., Alekhina, I. A., Blot, M., Petit, J. R., de Angelis, M., Wagenbach, D., Lipenkov, V. Y., Vasilyeva, L. P., Wloch, D. M., … Lukin, V. V. (2004). DNA signature of thermophilic bacteria from the aged accretion ice of Lake Vostok, Antarctica: Implications for searching for life in extreme icy environments. *Int. J. Astrobiol.*, *3*(1), 1–12. https://doi.org/10.1017/s1473550404001879

Carter, S. P., Blankenship, D. D., Young, D. A., and Holt, J. W. (2009). Using radar-sounding data to identify the distribution and sources of subglacial water: Application to Dome C, East Antarctica. *J. Glaciol.*, *55*(194), 1025–1040. https://doi.org/10.3189/002214309790794931

Cochran, J. R., Tinto, K. J., and Bell, R. E. (2020). Detailed bathymetry of the continental shelf beneath the Getz Ice Shelf, West Antarctica. *J. Geophys. Res.: Earth Surface*, *125*(10), e2019JF005493. https://doi.org/10.1029/2019jf005493

Couston, L. A., and Siegert, M. (2021). Dynamic flows create potentially habitable conditions in Antarctic subglacial lakes. *Sci. Adv.*, *7*(8), eabc3972. https://doi.org/10.1126/sciadv.abc3972

Cui, X. B., Greenbaum, J. S., Beem, L. H., Guo, J. X., Ng, G., Li, L., Blankenship, D., and Sun, B. (2018). The first fixed-wing aircraft for Chinese Antarctic expeditions: Airframe, modifications, scientific instrumentation and applications. *J. Environ. Eng. Geophys.*, *23*(1), 1–13. https://doi.org/10.2113/JEEG23.1.1

Cui, X. B., Jeofry, H., Greenbaum, J. S., Guo, J. X., Li, L., Lindzey, L. E., Habbal, F. A., Wei, W., Young, D. A., … Siegert, M. J. (2020). Bed topography of Princess Elizabeth Land in East Antarctica. *Earth Syst. Sci. Data*, *12*(4), 2765–2774. https://doi.org/10.5194/essd-12-2765-2020

de Q. Robin, G., Swithinbank, C., and Smith, B. M. E. (1970). Radio echo exploration of the Antarctic ice sheet. In A. J. Gow, et al. (Eds.), *International Symposium on Antarctic Glaciological Exploration* (*ISAGE*), *Hanover, New Hampshire, 3–7 September 1968* (pp. 97–115). Gentbrugge, Belgium: International Association of Scientific Hydrology.

Dow, C. F., Werder, M. A., Babonis, G., Nowicki, S., Walker, R. T., Csatho, B., and Morlighem, M. (2018). Dynamics of active subglacial lakes in Recovery Ice Stream. *J. Geophys. Res.: Earth Surf.*, *123*(4), 837–850. https://doi.org/10.1002/2017jf004409

Dowdeswell, J. A., and Evans, S. (2004). Investigations of the form and flow of ice sheets and glaciers using radio-echo sounding. *Rep. Prog. Phys.*, *67*(10), 1821–1861. https://doi.org/10.1088/0034-4885/67/10/r03

Duxbury, N. S., Zotikov, I. A., Nealson, K. H., Romanovsky, V. E., and Carsey, F. D. (2001). A numerical model for an alternative origin of Lake Vostok and its exobiological implications for Mars. *J. Geophys. Res.: Planets*, *106*(E1), 1453–1462. https://doi.org/10.1029/2000je001254

Fricker, H. A., Siegfried, M. R., Carter, S. P., and Scambos, T. A. (2016). A decade of progress in observing and modelling Antarctic subglacial water systems. *Philos. Trans. Roy. Soc. A: Math., Phys. Eng. Sci.*, *374*(2059), 20140294. https://doi.org/10.1098/rsta.2014.0294

Gorman, M. R., and Siegert, M. J. (1999). Penetration of Antarctic subglacial lakes by VHF electromagnetic pulses: Information on the depth and electrical conductivity of basal water bodies. *J. Geophys. Res.: Solid Earth*, *104*(B12), 29311–29320. https://doi.org/10.1029/1999jb900271

Haran, T., Klinger, M., Bohlander, J., Fahnestock, M., Painter, T., and Scambos, T. (2018). MEaSUREs MODIS mosaic of Antarctica 2013–2014 (MOA2014) Image Map, Version 1. Boulder, Colorado, USA: NASA National Snow and Ice Data Center Distributed Active Archive Center. https://doi.org/10.5067/RNF17BP824UM

Haran, T., Bohlander, J., Scambos, T., Painter, T., and Fahnestock, M. (2021a). MODIS Mosaic of Antarctica 2003–2004 (MOA2004) Image Map, Version 2. Boulder, Colorado, USA: NASA National Snow and Ice Data Center Distributed Active Archive Center. https://doi.org/10.5067/68TBT0CGJSOJ

Haran, T., Bohlander, J., Scambos, T., Painter, T., and Fahnestock, M. (2021b). MODIS Mosaic of Antarctica 2008–2009 (MOA2009) Image Map, Version 2. Boulder, Colorado, USA: NASA National Snow and Ice Data Center Distributed Active Archive Center. https://doi.org/10.5067/4ZL43A4619AF

Hills, B. H., Christianson, K., Hoffman, A. O., Fudge, T. J., Holschuh, N., Kahle, E. C., Conway, H., Christian, J. E., Horlings, A. N., … Steig, E. J. (2022). Geophysics and thermodynamics at South Pole Lake indicate stability and a regionally thawed bed. *Geophys. Res. Lett.*, *49*(2), e2021GL096218. https://doi.org/10.1029/2021gl096218

Howat, I. M., Porter, C., Smith, B. E., Noh, M. J., and Morin, P. (2019). The reference elevation model of Antarctica. *Cryosphere*, *13*(2), 665–674. https://doi.org/10.5194/tc-13-665-2019

Jamieson, S. S. R., Ross, N., Greenbaum, J. S., Young, D. A., Aitken, A. R. A., Roberts, J. L., Blankenship, D. D., Bo, S., and Siegert, M. J. (2016). An extensive subglacial lake and canyon system in Princess Elizabeth Land, East Antarctica. *Geology*, *44*(2), 87–90. https://doi.org/10.1130/g37220.1

Kapitsa, A. P., Ridley, J. K., de Q. Robin, G., Siegert, M. J., and Zotikov, I. A. (1996). A large deep freshwater lake beneath the ice of central East Antarctica. *Nature*, *381*(6584), 684–686. https://doi.org/10.1038/381684a0

Karl, D. M., Bird, D. F., Bjorkman, K., Houlihan, T., Shackelford, R., and Tupas, L. (1999). Microorganisms in the accreted ice of Lake Vostok, Antarctica. *Science*, *286*(5447), 2144–2147. https://doi.org/10.1126/science.286.5447.2144

Killingbeck, S. F., Rutishauser, A., Unsworth, M. J., Dubnick, A., Criscitiello, A. S., Killingbeck, J., Dow, C. F., Hill, T., Booth, A. D., … Brossier, E. (2024). Misidentified subglacial lake beneath the Devon Ice Cap, Canadian Arctic: A new interpretation from seismic and electromagnetic data. *Cryosphere*, *18*(8), 3699–3722. https://doi.org/10.5194/tc-18-3699-2024

Klokočník, J., Kostelecký, J., Cílek, V., Bezděk, A., and Pešek, I. (2018). Gravito-topographic signal of the Lake Vostok area, Antarctica, with the most recent data. *Polar Sci.*, *17*, 59–74. https://doi.org/10.1016/j.polar.2018.05.002

Kotlyakov, V. M., Vasiliev, L. N., Kachalin, A. B., Moskalevskii, M. Y., and Tyuflin, A. S. (2011). Punctuated equilibrium of the surface above subglacial Lake Vostok in Antarctica. *Dokl. Earth Sci.*, *438*(1), 649–651. https://doi.org/10.1134/s1028334x11050047

Lavire, C., Normand, P., Alekhina, I., Bulat, S., Prieur, D., Birrien, J. L., Fournier, P., Hänni, C., and Petit, J. R. (2006). Presence of *Hydrogenophilus thermoluteolus* DNA in accretion ice in the subglacial Lake Vostok, Antarctica, assessed using *rrs, cbb* and *hox*. *Environ. Microbiol.*, *8*(12), 2106–2114. https://doi.org/10.1111/j.1462-2920.2006.01087.x

Li, L., Tang, X. Y., Guo, J. X., Cui, X. B., Xiao, E. Z., Latif, K., Sun, B., Zhang, Q., and Shi, X. S. (2021). Inversion of geothermal heat flux under the ice sheet of Princess Elizabeth Land, East Antarctica. *Remote Sens.*, *13*(14), 2760. https://doi.org/10.3390/rs13142760

Livingstone, S. J., Li, Y., Rutishauser, A., Sanderson, R. J., Winter, K., Mikucki, J. A., Björnsson, H., Bowling, J. S., Chu, W., … Sole, A. J. (2022). Subglacial lakes and their changing role in a warming climate. *Nat. Rev. Earth Environ.*, *3*(2), 106–124. https://doi.org/10.1038/s43017-021-00246-9

Magnússon, E., Rott, H., Björnsson, H., and Pálsson, F. (2007). The impact of jökulhlaups on basal sliding observed by SAR interferometry on Vatnajökull, Iceland. *J. Glaciol.*, *53*(181), 232–240. https://doi.org/10.3189/172756507782202810

Magnússon, E., Björnsson, H., Rott, H., and Pálsson, F. (2010). Reduced glacier sliding caused by persistent drainage from a subglacial lake. *Cryosphere*,

4(1), 13–20. https://doi.org/10.5194/tc-4-13-2010

Maguire, R., Schmerr, N., Pettit, E., Riverman, K., Gardner, C., DellaGiustina, D. N., Avenson, B., Wagner, N., Marusiak, A. G., … Bailey, S. H. (2021). Geophysical constraints on the properties of a subglacial lake in northwest Greenland. *Cryosphere*, *15*(7), 3279–3291. https://doi.org/10.5194/tc-15-3279-2021

Martos, Y. M., Catalán, M., Jordan, T. A., Golynsky, A., Golynsky, D., Eagles, G., and Vaughan, D. G. (2017). Heat flux distribution of Antarctica unveiled. *Geophys. Res. Lett.*, *44*(22), 11417–11426. https://doi.org/10.1002/2017gl075609

Mayer, C., and Siegert, M. J. (2000). Numerical modelling of ice-sheet dynamics across the Vostok subglacial lake, central East Antarctica. *J. Glaciol.*, *46*(153), 197–205. https://doi.org/10.3189/172756500781832981

Millan, R., St-Laurent, P., Rignot, E., Morlighem, M., Mouginot, J., and Scheuchl, B. (2020). Constraining an ocean model under Getz Ice Shelf, Antarctica, using a gravity-derived bathymetry. *Geophys. Res. Lett.*, *47*(13), e2019GL086522. https://doi.org/10.1029/2019GL086522

Morlighem, M., Williams, C. N., Rignot, E., An, L., Arndt, J. E., Bamber, J. L., Catania, G., Chauché, N., Dowdeswell, J. A., … Zinglersen, K. B. (2017). BedMachine v3: Complete bed topography and ocean bathymetry mapping of Greenland from multibeam echo sounding combined with mass conservation. *Geophys. Res. Lett.*, *44*(21), 11051–11061. https://doi.org/10.1002/2017gl074954

Napoleoni, F., Jamieson, S. S. R., Ross, N., Bentley, M. J., Rivera, A., Smith, A. M., Siegert, M. J., Paxman, G. J. G., Gacitúa, G., … Vaughan, D. G. (2020). Subglacial lakes and hydrology across the Ellsworth Subglacial Highlands, West Antarctica. *Cryosphere*, *14*(12), 4507–4524. https://doi.org/10.5194/tc-14-4507-2020

Petit, J. R., Jouzel, J., Raynaud, D., Barkov, N. I., Barnola, J. M., Basile, I., Bender, M., Chappellaz, J., Davis, M., … Stiévenard, M. (1999). Climate and atmospheric history of the past 420,000 years from the Vostok ice core, Antarctica. *Nature*, *399*(6735), 429–436. https://doi.org/10.1038/20859

Popov, S. (2022). Ice cover, subglacial landscape, and estimation of bottom melting of Mac. Robertson, Princess Elizabeth, Wilhelm II, and western Queen Mary Lands, East Antarctica. *Remote Sens.*, *14*(1), 241. https://doi.org/10.3390/rs14010241

Purucker, M. (2013). Geothermal heat flux data set based on low resolution observations collected by the CHAMP satellite between 2000 and 2010, and produced from the MF-6 model following the technique described in Fox Maule et al. (2005). *Interact. Syst. Ice Sheet Simul.* https://core2.gsfc.nasa.gov/research/purucker/heatflux_updates.html (last access: 4 June 2025)

Richter, A., Popov, S. V., Dietrich, R., Lukin, V. V., Fritsche, M., Lipenkov, V. Y., Matveev, A. Y., Wendt, J., Yuskevich, A. V., and Masolov, V. N. (2008). Observational evidence on the stability of the hydro-glaciological regime of subglacial Lake Vostok. *Geophys. Res. Lett.*, *35*(11), L11502. https://doi.org/10.1029/2008gl033397

Richter, A., Schröder, L., Scheinert, M., Popov, S. V., Groh, A., Willen, M., Horwath, M., and Dietrich, R. (2022). The hydrostatic control of load-induced height changes above subglacial Lake Vostok. *J. Glaciol.*, *68*(271), 849–866. https://doi.org/10.1017/jog.2022.2

Rignot, E., Mouginot, J., and Scheuchl, B. (2017). MEaSUREs InSAR-Based Antarctica Ice Velocity Map, Version 2. Boulder, Colorado, USA: NASA National Snow and Ice Data Center Distributed Active Archive Center. https://doi.org/10.5067/D7GK8F5J8M8R

Rivera, A., Uribe, J., Zamora, R., and Oberreuter, J. (2015). Subglacial Lake CECs: Discovery and in situ survey of a privileged research site in West Antarctica. *Geophys. Res. Lett.*, *42*(10), 3944–3953. https://doi.org/10.1002/2015gl063390

Schroeder, D. M., Blankenship, D. D., and Young, D. A. (2013). Evidence for a water system transition beneath Thwaites Glacier, West Antarctica. *Proc. Natl. Acad. Sci. USA*, *110*(30), 12225–12228. https://doi.org/10.1073/pnas.1302828110

Schwabe, J., Ewert, H., Scheinert, M., and Dietrich, R. (2014). Regional geoid modeling in the area of subglacial Lake Vostok, Antarctica. *J. Geodyn.*, *75*, 9–21. https://doi.org/10.1016/j.jog.2013.12.002

Shen, W. S., Wiens, D. A., Lloyd, A. J., and Nyblade, A. A. (2020). A geothermal heat flux map of Antarctica empirically constrained by seismic structure. *Geophys. Res. Lett.*, *47*(14), e2020GL086955. https://doi.org/10.1029/2020gl086955

Siegert, M. J., and Ridley, J. K. (1998). An analysis of the ice-sheet surface and subsurface topography above the Vostok Station subglacial lake, central East Antarctica. *J. Geophys. Res.: Solid Earth*, *103*(B5), 10195–10207. https://doi.org/10.1029/98jb00390

Siegert, M. J. (2000). Antarctic subglacial lakes. *Earth-Sci. Rev.*, *50*(1-2), 29–50. https://doi.org/10.1016/S0012-8252(99)00068-9

Siegert, M. J. (2002). Which are the most suitable Antarctic subglacial lakes for exploration?. *Polar Geogr.*, *26*(2), 134–146. https://doi.org/10.1080/789610135

Siegert, M. J., Carter, S., Tabacco, I., Popov, S., and Blankenship, D. D. (2005). A revised inventory of Antarctic subglacial lakes. *Antarct. Sci.*, *17*(3), 453–460. https://doi.org/10.1017/s0954102005002889

Siegert, M. J., Popov, S., and Studinger, M. (2011). Vostok subglacial lake: A review of geophysical data regarding its discovery and topographic setting. In M. J. Siegert, et al. (Eds.), *Antarctic Subglacial Aquatic Environments* (pp. 45–60). Washington, DC: American Geophysical Union. https://doi.org/10.1002/9781118670354.ch4

Siegfried, M. R., Fricker, H. A., Carter, S. P., and Tulaczyk, S. (2016). Episodic ice velocity fluctuations triggered by a subglacial flood in West Antarctica. *Geophys. Res. Lett.*, *43*(6), 2640–2648. https://doi.org/10.1002/2016gl067758

Smith, A. M., Woodward, J., Ross, N., Bentley, M. J., Hodgson, D. A., Siegert, M. J., and King, E. C. (2018). Evidence for the long-term sedimentary environment in an Antarctic subglacial lake. *Earth Planet. Sci. Lett.*, *504*, 139–151. https://doi.org/10.1016/j.epsl.2018.10.011

Studinger, M., Bell, R. E., Karner, G. D., Tikku, A. A., Holt, J. W., Morse, D. L., Richter, T. G., Kempf, S. D., Peters, M. E., ... Rystrom, V. L. (2003a). Ice cover, landscape setting, and geological framework of Lake Vostok, East Antarctica. *Earth and Planetary Science Letters*, *205*(3-4), 195–210. https://doi.org/10.1016/S0012-821X(02)01041-5

Studinger, M., Karner, G. D., Bell, R. E., Levin, V., Raymond, C. A., and Tikku, A. A. (2003b). Geophysical models for the tectonic framework of the Lake Vostok region, East Antarctica. *Earth Planet. Sci. Lett.*, *216*(4), 663–677. https://doi.org/10.1016/s0012-821x(03)00548-x

Studinger, M., Bell, R. E., and Tikku, A. A. (2004). Estimating the depth and shape of subglacial Lake Vostok's water cavity from aerogravity data. *Geophys. Res. Lett.*, *31*(12), L12401. https://doi.org/10.1029/2004gl019801

Talwani, M., Worzel, J. L., and Landisman, M. (1959). Rapid gravity computations for two-dimensional bodies with application to the Mendocino submarine fracture zone. *J. Geophys. Res.*, *64*(1), 49–59. https://doi.org/10.1029/JZ064i001p00049

Thoma, M., Grosfeld, K., and Mayer, C. (2007). Modelling mixing and circulation in subglacial Lake Vostok, Antarctica. *Ocean Dyn.*, *57*(6), 531–540. https://doi.org/10.1007/s10236-007-0110-9

Wingham, D. J., Siegert, M. J., Shepherd, A., and Muir, A. S. (2006). Rapid discharge connects Antarctic subglacial lakes. *Nature*, *440*(7087), 1033–1036. https://doi.org/10.1038/nature04660

Yan, S., Blankenship, D. D., Greenbaum, J. S., Young, D. A., Li, L., Rutishauser, A., Guo, J. X., Roberts, J. L., van Ommen, T. D., … Sun, B. (2022). A newly discovered subglacial lake in East Antarctica likely hosts a valuable sedimentary record of ice and climate change. *Geology*, *50*(8), 949–953. https://doi.org/10.1130/g50009.1

Yang, J. J., Guo, J. X., Greenbaum, J. S., Cui, X. B., Tu, L. C., Li, L., Jong, L. M., Tang, X. Y., Li, B. R., … Sun, B. (2021). Bathymetry beneath the Amery Ice Shelf, East Antarctica, revealed by airborne gravity. *Geophys. Res. Lett.*, *48*(24), e2021GL096215. https://doi.org/10.1029/2021gl096215

Young, D. A., Schroeder, D. M., Blankenship, D. D., Kempf, S. D., and Quartini, E. (2016). The distribution of basal water between Antarctic subglacial lakes from radar sounding. *Philos. Trans. Roy. Soc. A: Math., Phys. Eng. Sci.*, *374*(2059), 20140297. https://doi.org/10.1098/rsta.2014.0297